water

MDPI

Article

Surge Response and Double-Peak Formation Mechanism in a Throttled Surge Tank with a Lateral Chamber

Herui Liu [1], Minglei Shao [1,*], Yin Liu [1], Ziyang Zhang [1], Rongchuan Kong [2], Dongshen Yang [1], Botao Hu [1], Jing Kang [1] and Yupeng Yan [1]

[1] PowerChina Northwest Engineering Corporation Limited, Xi'an 710100, China; herui.liu@whu.edu.cn (H.L.); ly02283@nwh.cn (Y.L.); xby03430@powerchina.cn (Z.Z.); yangdongsheng@nwh.cn (D.Y.); djxbbht@126.com (B.H.); kangjing@zgdjxby.wecom.work (J.K.); 17300860528@163.com (Y.Y.)
[2] College of Water Conservancy and Hydropower Engineering, Hohai University, Nanjing 210098, China; 251302030029@hhu.edu.cn
* Correspondence: liuher@nwh.cn; Tel.: +86-15623906603

Abstract

Lateral chambers increase surge-tank storage, but horizontal free-surface motion can delay their participation in transient water redistribution. A water–air volume-of-fluid model was used to investigate throttled surge tanks without a lateral chamber and with 40 m and 80 m chambers. Volume-equivalent shaft levels and sectional depths were combined with a quasi-static reference at equal instantaneous water volume, water-volume balances, and proper orthogonal decomposition (POD). Under identical imposed discharge histories, the 80 m chamber reduced the maximum shaft level by 6.15 m relative to the configuration without a chamber, but lowered the subsequent minimum by 3.56 m. The 40 m case exhibited two peaks with a secondary-to-primary amplitude ratio of 0.734. Between the intervening minimum and the secondary peak, chamber release supplied 231.1 m^3 against 90.1 m^3 of net external outflow, producing an actual main-domain gain of 146.3 m^3. Chamber storage maxima lagged the shaft peaks by 9.4 s and 10 s. The first two POD modes represented 89.7% and 86.6% of depth-fluctuation mean-square content. These results link surge-waveform formation to delayed storage and return flow. The findings provide a physical basis for understanding the transient behavior and hydraulic design of throttled surge tanks with lateral chambers.

Keywords: throttled surge tank; lateral chamber; surge response; free-surface propagation; pump-turbine

Check for updates

Academic Editor: Mouldi Ben Meftah

Received: 9 October 2026
Revised: 28 October 2026
Accepted: 30 October 2026
Published: 31 October 2026

Copyright: © 2026 by the authors. Licensee MDPI, Basel, Switzerland. This article is an open access article distributed under the terms and conditions of the Creative Commons Attribution (CC BY) license.

1. Introduction

Rapid starts and stops, load rejection, and emergency shutdowns in pumped-storage plants induce substantial hydraulic transients. Maximum and minimum surge-tank levels, together with their evolution, constrain underground waterway layouts and operational safety. Recent research has extended beyond extreme-level prediction for conventional tanks to the coordinated design of complex geometries and flexible operation. Tesfay et al. [1] investigated composite surge tanks for improving hydraulic transient performance and operational flexibility. Lan et al. [2] optimized a coaxial-shaft surge tank using physical-model tests, while Kheav et al. [3] compared air-chamber and orifice-type surge tanks under successive load rejection. These studies show that both additional storage and local hydraulic connections affect surge control; geometric capacity alone does not determine transient performance.

Surge waveforms also depend on waterway inertia, operating sequences, and local connections. Liu et al. [4] analyzed composite surge responses in two tanks connected in series; Cui and Guo [5] examined energy coupling and surge-wave superposition; and Wang et al. [6] investigated minimum tank levels and control timing during load acceptance after rejection. For a surge tank connected through a long lateral pipe, Zhang et al. [7] showed that pipe inertia and losses modify system stability. The dimensionless impedance and response analyses of Kim and Choi [8] and Kim [9] emphasize the need to match evaluation parameters to the hydraulic connection and characteristic scales. However, system-scale superposition in series-connected tanks and pressure oscillations in long connecting pipes differ from local responses involving free-surface propagation and reflection in a lateral chamber. Their conclusions cannot be transferred without examining the relevant flow processes.

Local hydraulic losses connect three-dimensional (3D) tank hydraulics with system-scale transient prediction. Seyfeddine et al. [10] combined one-dimensional (1D) transient modeling, physical tests, computational fluid dynamics (CFD), and prototype measurements in a holistic design approach for a throttled surge tank. Zhou et al. [11] reproduced 12 characteristic flow regimes at a surge-tank junction and established throttle-loss relationships dependent on flow regime and discharge ratio. Ma et al. [12] combined physical experiments and CFD to develop dynamic discharge coefficients for refined 1D plant simulations; their case study showed a 1.69 m difference in predicted water level relative to the traditional coefficient treatment. Gabl and Righetti [13] used CFD to examine how the radius, length, and entrance angle of an asymmetric orifice affect local head losses and the loss-coefficient ratio between opposite flow directions, providing guidance for orifice design. Adam et al. [14] systematically tested chamfered and rounded orifices and developed empirical relationships for estimating head-loss coefficients in both flow directions from orifice geometry. Zhang and Cheng [15] coupled a 1D hydraulic-transient model for pipeline sections with a 3D flow model for locally complex regions and assessed the approach using water-hammer and surge-tank oscillation cases. Cai et al. [16] examined how water inertia, hydraulic losses, and reservoir boundary conditions affect surge-level predictions, emphasizing the importance of friction-loss representation in long waterways. These studies establish a basis for relating local hydraulics to system response. Interpreting chamber transients further requires distinguishing representative shaft levels, longitudinal chamber depths, and local end-wall run-up.

Elongated or lateral chambers combine horizontal water migration with vertical shaft oscillation. Qiu et al. [17] developed and experimentally validated a model incorporating both vertical and horizontal water-level oscillations, demonstrating that horizontal motion cannot always be represented by lumped storage. Pagliaroli et al. [18] used POD and related methods to identify spatiotemporal structures in sloshing, while Bardazzi et al. [19] investigated different nonlinear sloshing regimes. These studies provide a basis for relating global signals to spatial responses. A single nonperiodic chamber transient includes an advancing wetting front, end-wall surface adjustment, and return flow. It should therefore be analyzed through event timing and spatial structure rather than by directly adopting natural-frequency or damping estimates from periodic sloshing. POD extracts dominant correlated structures using orthogonal basis functions, following the coherent-structure formulation of Sirovich [20].

Building on previous studies of horizontal water-level oscillations, this study links delayed lateral storage and return flow to surge-waveform formation using three-dimensional water–air simulations of a throttled surge tank without a lateral chamber and with 40 m and 80 m chambers. An equal-volume quasi-static reference distinguishes geometric capacity from its transient hydraulic participation. A partitioned water-volume balance identifies

delayed chamber return flow as the source of the secondary shaft-level rise in the 40 m case despite concurrent net external outflow. Wetting-front timing, flow fields, and proper orthogonal decomposition connect this mechanism to local water redistribution. These contributions provide a quantitative explanation of asynchronous shaft–chamber responses and double-peak formation, supporting performance assessment based on both surge extrema and the timing of storage exchange.

2. Materials and Methods

2.1. Engineering Layout and Computational Geometries

The study concerns a throttled surge tank in the tailrace system of a pumped-storage plant in Xinjiang, China. The project layout comprises a 7.4 m diameter tailrace tunnel with a 23.7 m horizontal reach and a 785.0 m inclined reach at 5°. The main shaft and connecting pipe have diameters of 10.0 m and 4.9 m, respectively. The lateral chamber has an arched cross-section 6.0 m wide and 8.0 m high. An upper chamber at the shaft crest connects to the atmosphere through a ventilation tunnel. These project lengths describe the full waterway; the three-dimensional meshes represent a truncated local domain, as shown in Figures 1 and 2.

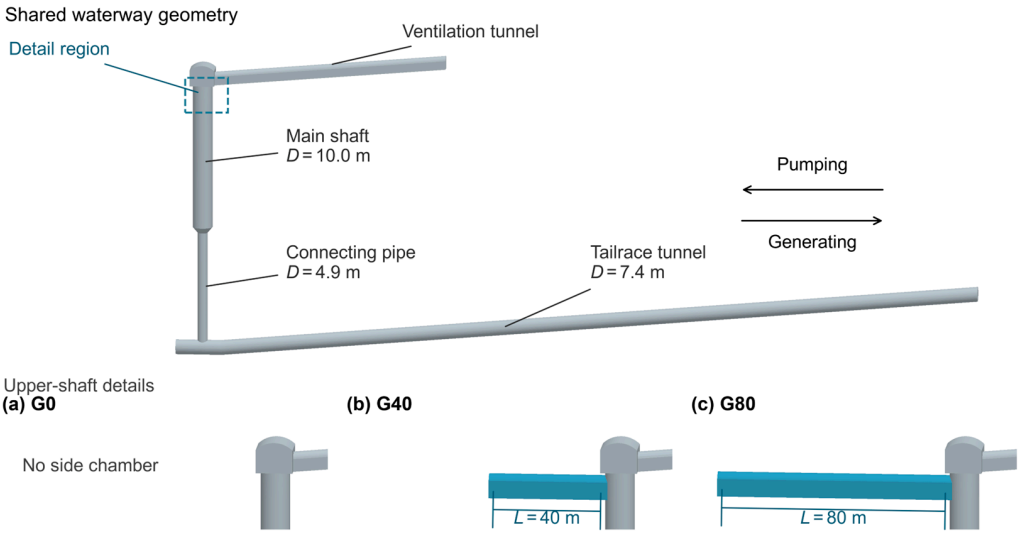

Figure 1. Three-dimensional geometries of the surge tank configurations. The (**upper**) panel shows the common waterway and shaft layout, and the dashed box identifies the chamber-junction detail. The (**lower**) panels show (**a**) G0, (**b**) G40, and (**c**) G80 using the same view and spatial scale. Gray denotes the common structures and blue denotes the lateral chamber. D is the diameter, and L is the chamber length measured from the outer shaft wall.

The configurations without a lateral chamber and with 40 m and 80 m chambers are designated G0, G40, and G80, respectively. Table 1 summarizes their dimensions. The local coordinates place the shaft axis at $x = y = 0$, with the lateral chamber extending in the positive x-direction. The chamber invert is at $z = 68$ m and the centerline crown at $z = 76$ m. Chamber length is measured from the outer shaft wall at $x = 5$ m; the end walls are therefore at $x = 45$ m for G40 and $x = 85$ m for G80. The shaft level is referenced to the chamber invert as $\eta = z - 68$ m.

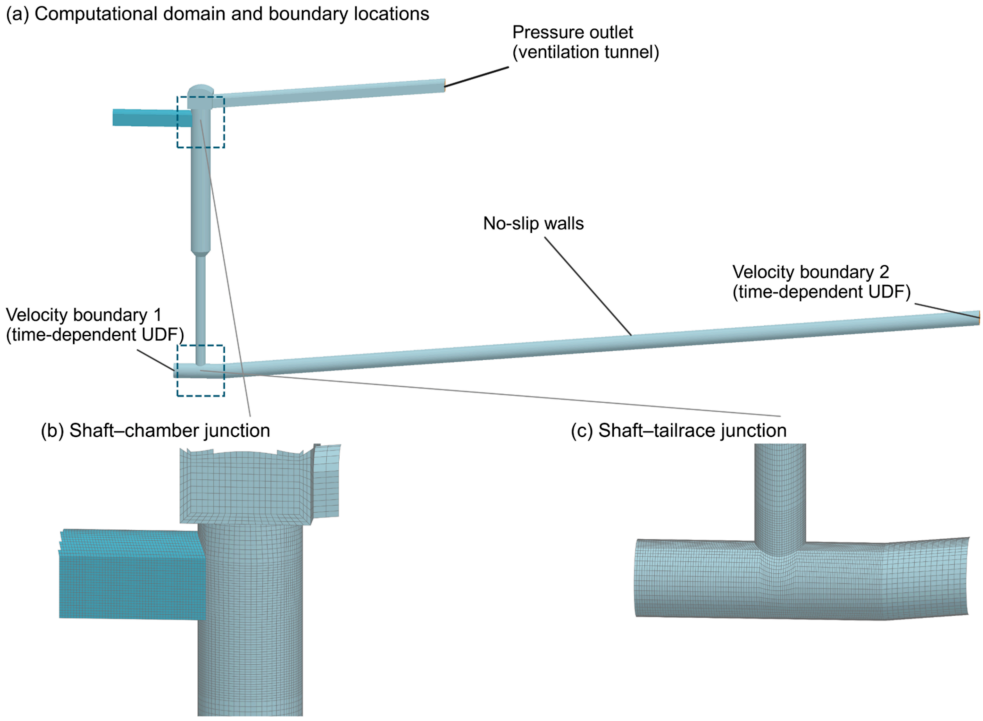

Figure 2. Computational domain, boundary conditions, and representative local meshes for G40: (**a**) domain and boundary locations; (**b**) shaft–chamber junction; and (**c**) shaft–tailrace junction. The enlarged panels show boundary-face meshes extracted from the case file. The two waterway boundaries receive time-dependent velocities through user-defined functions (UDFs); the ventilation boundary is a pressure outlet.

Table 1. Geometric parameters of the three configurations.

Parameter	G0	G40	G80
Chamber length (m)	0	40	80
Main-shaft diameter (m)	10.0	10.0	10.0
Connecting-pipe diameter (m)	4.9	4.9	4.9
Chamber width × height (m)	—	6.0 × 8.0	6.0 × 8.0
External chamber volume (m^3)	—	1786.1	3572.9

2.2. Meshes and Boundary Conditions

Hexahedral meshes were used throughout the computational domains. G0, G40, and G80 contain 1,027,312, 901,339, and 2,450,086 cells, respectively. Figure 2 shows the boundary locations and representative surface meshes around the shaft–chamber and shaft–tailrace junctions, where local flow changes and interface motion require resolution.

Time-dependent velocity conditions were prescribed at the two truncated waterway sections. Discharge histories from a one-dimensional hydraulic transient calculation were converted to velocities using the boundary areas and imposed through user-defined functions (UDFs). Velocity boundaries 1 and 2 in Figure 2 identify locations, and the actual flow direction can reverse during the transient. A pressure outlet was assigned to the ventilation-tunnel end, and solid boundaries were treated as no-slip walls. The initial water and air regions were specified through volume-fraction initialization. The operating condition, designated CP4, corresponds to the upper reservoir at dead-water level and the lower reservoir at normal storage level. Within one hydraulic unit, operation changes from one pumping unit to two pumping units, followed by sudden power failure at approximately 50 s with failure of guide-vane actuation. Water discharge into the computational domain is

defined as positive. G0 and G80 use the same prescribed discharge sequences and provide the controlled forcing comparison.

2.3. Governing Equations for Water–Air Flow

The three-dimensional flow simulations were performed using ANSYS Fluent 2022 R1. The volume-of-fluid (VOF) method was adopted for incompressible water–air flow [21]. The phases share a velocity field, and the water volume fraction α_w identifies the interface: $\alpha_w = 1$ denotes water, $\alpha_w = 0$ denotes air, and $0 < \alpha_w < 1$ denotes interfacial cells. The air volume fraction is $1 - \alpha_w$. With no phase change, water transport and velocity continuity are expressed as

$$\frac{\partial \alpha_w}{\partial t} + \nabla \cdot (\alpha_w u) = 0; \quad \nabla \cdot u = 0 \tag{1}$$

The mixture properties are weighted by volume fraction:

$$\rho = \alpha_w \rho_w + (1 - \alpha_w)\rho_a; \quad \mu = \alpha_w \mu_w + (1 - \alpha_w)\mu_a \tag{2}$$

The unsteady Reynolds-averaged momentum equation with eddy-viscosity closure is written as

$$\frac{\partial (\rho u)}{\partial t} + \nabla \cdot (\rho u \otimes u) = -\nabla p^* + \nabla \cdot [(\mu + \mu_t)(\nabla u + \nabla u^T)] + \rho g + f_\sigma \tag{3}$$

where u is the shared mean velocity vector; ρ and μ are mixture density and dynamic viscosity; μ_t is turbulent viscosity; $p^* = p + 2\rho k/3$ includes the isotropic turbulent stress; k is turbulent kinetic energy; g is gravitational acceleration; and f_σ is the volumetric surface-tension force. The water and air densities were set to $\rho_w = 998.2\ \mathrm{kg/m^3}$ and $\rho_a = 1.225\ \mathrm{kg/m^3}$, respectively. A gravitational acceleration of $9.81\ \mathrm{m/s^2}$ was applied in the negative z-direction, and the operating pressure was 101,325 Pa. The surface-tension coefficient was set to 0.013 N/m in G0 and G80 and zero in G40; consequently, f_σ vanishes in G40.

Turbulence was represented by the realizable k–ε model [22] with non-equilibrium wall functions. This formulation describes the transient mean flow; it does not directly resolve bubble-scale motion or all turbulent structures.

The numerical time-step settings are 0.02 s for G0 and 0.01 s for the later G40 calculation. The G80 case sequence uses 0.03 s, followed by 0.01 s and 0.005 s. Field snapshots in the interval analyzed here are available at approximately 0.2 s for G40 and 1 s for G0 and G80. Event times reported below refer to the available output, and the common 1 s sampling in the POD analysis is a post-processing interval rather than the solver time step.

3. Surge Evaluation and Flow-Field Analysis

3.1. Shaft Level and Dynamic Departure

A central sampling column C of radius R = 4 m was defined within the main shaft. Cells were selected by their centers within $3 < z < 86$ m. This selection excludes the lateral chamber and reduces contamination by localized interfaces near the shaft wall. The water volume and geometric hydrostatic capacity function are defined as

$$V_C(t) = \Sigma \alpha_{w,i}(t) V_i; C_C(z) = \Sigma V_i \varphi_i(z)\ (i \in C) \tag{4}$$

$$\eta(t) = {C_C}^{-1}[V_C(t)] - z_b \tag{5}$$

where V_i is cell volume and $z_b = 68$ m. The geometric occupancy fraction $\varphi_i(z)$ is zero below the lowest cell node and unity above the highest node. For an intersected cell, a linear occupancy approximation is used over its vertical nodal extent. Thus, η is a volume-equivalent shaft level rather than maximum local end-wall run-up. Sampling radii of 3 m and 4.5 m were also examined to assess the sensitivity of this extraction procedure.

An analogous capacity function C_Ω is constructed for the entire domain Ω. A horizontal quasi-static reference level η_{qs} is obtained by retaining the actual instantaneous total water volume $V_w(t)$. The dynamic level departure Δη and its normalized index I_d are defined as

$$\eta_{qs}(t) = C_\Omega{}^{-1}[V_w(t)] - z_b \quad (6)$$

$$\Delta\eta(t) = \eta(t) - \eta_{qs}(t) \quad (7)$$

$$I_d(t) = \frac{\Delta\eta(t)}{H_e} \quad (8)$$

The common chamber-height scale is $H_e = 8$ m, including for G0. Both Δη and I_d are invariant to a shift in the elevation datum. Normalization by H_e also avoids an unstable ratio when the quasi-static level is close to zero. A positive departure indicates a shaft level above the equal-volume horizontal reference; a negative departure indicates that relatively more water is distributed outside the shaft. For a discernible double peak, the first peak η_{p1}, second peak η_{p2}, and intervening minimum η_m define the secondary-to-primary amplitude ratio:

$$K_2 = \frac{\eta_{p2} - \eta_m}{\eta_{p1} - \eta_m} \quad (9)$$

The ratio uses the common intervening minimum as its amplitude reference. A value of $K_2 = 1$ indicates equal peak amplitudes relative to that minimum. It describes double-peak morphology and is not a wave-reflection coefficient obtained by separating incident and reflected waves.

3.2. Chamber Depth and Sectional Flow State

The chamber is divided into longitudinal segments of Δs = 1 m. Equivalent depth h(s, t) is obtained by inverting the segment water volume against its geometric capacity. Integrating over the full chamber length, including dry segments with zero depth, gives a longitudinal depth standard deviation normalized by structural height:

$$\bar{h}(t) = \frac{1}{L}\int_0^L h(s,t)\,ds; \; I_h(t) = \frac{\sqrt{\frac{1}{L}\int_0^L \left[h(s,t) - \bar{h}(t)\right]^2 ds}}{H_e} \quad (10)$$

The index I_h measures longitudinal depth nonuniformity, including both wet–dry contrasts associated with the advancing front and surface adjustment within wetted regions. The fixed scale H_e avoids the instability of a coefficient of variation when mean depth approaches zero; a separate depth coefficient of variation is therefore unnecessary. Segments with h > 0.1 m are classified as wetted, and the front position is the center of the furthest wetted segment. The equivalent area, hydraulic depth, and sectional Froude number are calculated as

$$A(h) = \frac{V_{w,\Delta s}}{\Delta s} \quad (11)$$

$$T(h) = \frac{dA}{dh} \quad (12)$$

$$D_h = \frac{A}{T} \quad (13)$$

$$Fr = \frac{|u|}{\sqrt{gD_h}} \quad (14)$$

where A is the equivalent wetted area; T is the free-surface width obtained by differentiating the sectional capacity with respect to depth; D_h is hydraulic depth; and ū is the water-volume-weighted longitudinal velocity of a segment. Fr characterizes partially filled free-surface sections under approximately hydrostatic conditions. Dry segments, nearly full sections with vanishing surface width, and strongly nonhydrostatic regions are excluded from shallow-water critical-flow interpretation.

3.3. Partitioned Water-Volume Balance and Storage Trajectories

The chamber outside the shaft wall is designated S, and the remainder of the domain is M, such that $V_w = V_M + V_S$. Because the chamber has no separate external water-flow boundary, its net exchange discharge Q_S is obtained from the change in stored water volume. Positive Q_S denotes flow into the chamber and negative Q_S denotes return flow to the main domain. Capacity utilization U_v and the partitioned continuity relations are defined as

$$U_v(t) = \frac{V_S(t)}{V_{S,geom}};\ Q_S = \frac{dV_S}{dt};\ \frac{dV_M}{dt} = Q_{net} - Q_S \tag{15}$$

Here, $V_{S,geom}$ is the chamber geometric volume. Net external water discharge Q_{net} is reconstructed from the boundary-face mixture mass flux, mixture density, and water volume fraction; ventilation-air exchange is not counted as water flow. To avoid amplifying errors through snapshot-volume differentiation, the secondary-peak mechanism is evaluated using cumulative volumes between the intervening minimum at t_v and the secondary peak at t_2:

$$V_M(t_2) - V_M(t_v) = \int_{t_v}^{t_2} Q_{net}(t)\,dt + V_S(t_v) - V_S(t_2) + \varepsilon_V \tag{16}$$

The residual ε_V includes sparse temporal integration, field extraction, and numerical errors in the balance reconstructed from the available flow-field snapshots. Storage trajectories use η/H_e and U_v as coordinates, with color and arrows indicating time and evolution direction. These trajectories identify the asynchronous response of shaft level and chamber storage.

3.4. POD of Spatiotemporal Depth Structures

Equivalent depths over 60–95 s are linearly resampled to a common 1 s interval, and the temporal mean at each longitudinal position is removed. POD is performed using a spatially averaged inner product [18,20]:

$$h'(s,t) = h(s,t) - \langle h(s,t)\rangle_t = \sum_{k=1}^{r} a_k(t)\phi_k(s) \tag{17}$$

$$\frac{1}{L}\int_0^L \phi_i\phi_j\,ds = \delta_{ij} \tag{18}$$

$$r_k = \frac{{\sigma_k}^2}{\sum_{j=1}^{r} {\sigma_j}^2} \tag{19}$$

$$\varepsilon_m = \frac{\|h' - \sum_{k=1}^{m} a_k\phi_k\|}{\|h'\|} = \sqrt{1 - \sum_{k=1}^{m} r_k} \tag{20}$$

The quantities a_k, ϕ_k, and σ_k are the temporal coefficient, spatial mode, and singular value, respectively, and r is the data-matrix rank. The modal fraction r_k represents depth-fluctuation mean-square content. The relative m-mode reconstruction error ε_m is the Frobenius norm of the residual divided by that of the original fluctuation matrix on the same space–time grid; both norms in Equation (20) are matrix Frobenius norms. Spatial modes are dimensionless and temporal coefficients have units of meters. The first two modes, their coefficient trajectories, and the reconstruction residuals are examined. Each case is decomposed independently, with the mode sign selected to make its largest absolute extremum positive. Identical mode numbers do not establish identical natural vibration modes, and r_k is not a mechanical-energy fraction.

Centerplane flow fields at y = 0 are interpolated from the original cell fields using inverse-squared-distance weighting over eight nearest neighbors, with a geometric mask excluding points outside the domain. The $\alpha_w = 0.5$ contour identifies the free surface. Velocity magnitude and in-plane direction arrows are displayed only where $\alpha_w \geq 0.5$. All water-volume, POD, and sectional-flow metrics are calculated from original-cell integrals and segment geometry; interpolated plots are used only to interpret spatial flow patterns.

4. Results

4.1. Upward and Downward Surges and Dynamic Departure

Figure 3 combines the complete shaft-level histories, local double-peak structure, dynamic departures, and storage responses. Under the same prescribed discharge histories, the maximum shaft levels in G0 and G80 are 10.38 m and 4.23 m at approximately 71 s and 67 s, respectively: a reduction of 6.15 m. Their subsequent minimum levels at approximately 113 s are −32.74 m and −36.31 m, respectively, with G80 lower by 3.56 m when calculated from the unrounded data. Thus, the chamber lowers both the upward-surge maximum and the downward-surge minimum, producing different implications for the two design constraints.

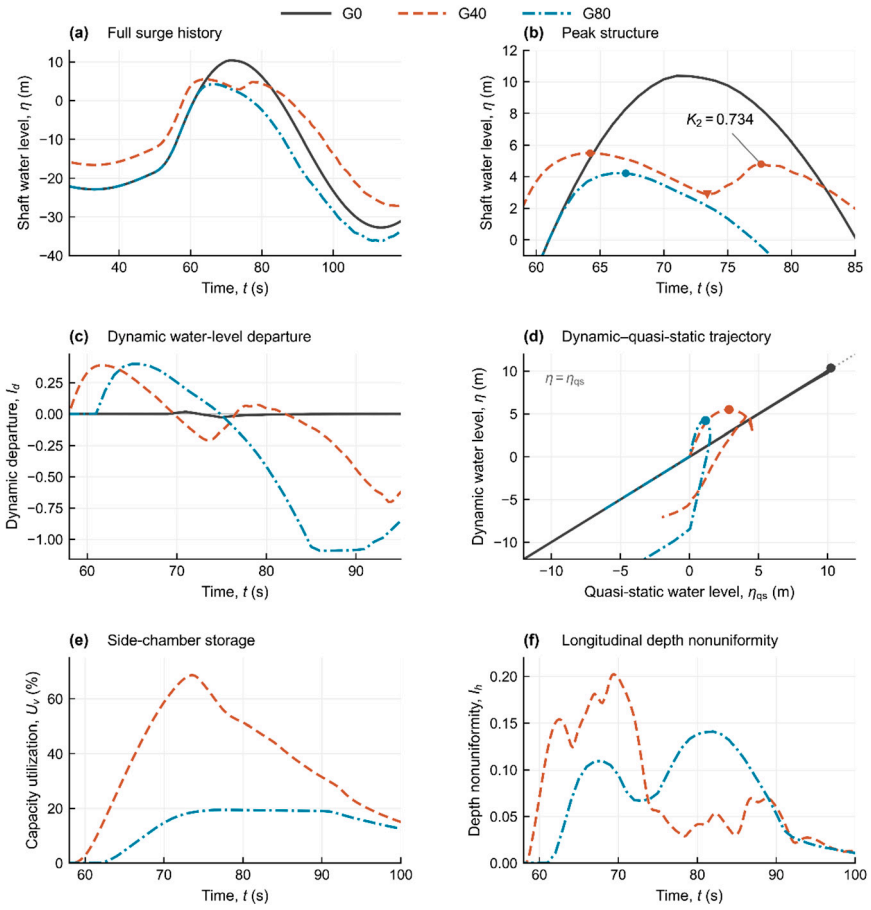

Figure 3. Relationships between shaft surges and dynamic chamber responses: (**a**) complete upward and downward surge histories; (**b**) primary-peak structure and the G40 double peak; (**c**) normalized dynamic departure from the equal-volume reference; (**d**) dynamic versus quasi-static level trajectories, with points marking the shaft maxima; (**e**) capacity utilization; and (**f**) longitudinal depth nonuniformity.

G40 develops two shaft-level peaks: 5.50 m at 64.21 s and 4.81 m at 77.60 s. The intervening minimum is 2.90 m at 73.40 s. The resulting amplitude ratio is $K_2 = 0.734$, indicating a lower secondary peak. The maximum positive dynamic departures are approximately 0.14 m for G0, 3.12 m for G40, and 3.20 m for G80, giving maximum I_d values of approximately 0.018, 0.390, and 0.400, respectively. These departure maxima are evaluated over 55–100 s. G0 remains close to the equal-volume reference, whereas the chamber-case trajectories depart markedly from the $\eta = \eta_{qs}$ diagonal. A horizontal, instantaneously equilibrated storage relation therefore does not describe the association between shaft level and total domain water volume in the two chamber cases. Table 2 summarizes the metrics.

Table 2. Shaft-surge and dynamic-departure metrics.

Metric	G0	G40	G80
Maximum shaft level (m)	10.38	5.50	4.23
Time of maximum level (s)	71	64.21	67
Minimum shaft level (m)	−32.74	−27.13	−36.31
Maximum positive I_d	0.018	0.390	0.400
Secondary-to-primary amplitude ratio K_2	—	0.734	—

Note: Maximum positive I_d is evaluated over 55–100 s. Peak levels are referenced to the chamber invert.

4.2. Storage Lag and Water Supply to the Secondary Rise

Figure 3e shows maximum chamber water volumes of 1225.5 m^3 for G40 and 694.9 m^3 for G80, corresponding to capacity utilizations of 68.6% and 19.4%. Storage maxima occur at 73.60 s and 77 s, respectively, approximately 9.4 s and 10 s after the shaft peaks. Thus, the chamber can continue accepting water after the shaft level has begun to fall.

Figure 4a,b presents the main-domain balance between the intervening minimum and secondary peak in G40. The chamber releases 231.1 m^3 while net external inflow is −90.1 m^3, indicating net outflow. Their combination reconstructs a main-domain gain of 140.9 m^3, compared with an actual gain of 146.3 m^3; the residual is 5.4 m^3. The secondary rise is therefore associated with chamber return flow supplying the main domain while the external boundaries continue to remove water. The time-colored trajectories in Figure 4c,d also show that storage is not a single-valued function of shaft level. After the shaft maximum, each trajectory continues toward higher U_v, then turns near maximum chamber storage. G40 exhibits another shaft-level rise during the secondary-peak stage. G80 retains substantial chamber water after the shaft level has fallen appreciably, demonstrating different response times for horizontal redistribution and vertical shaft motion.

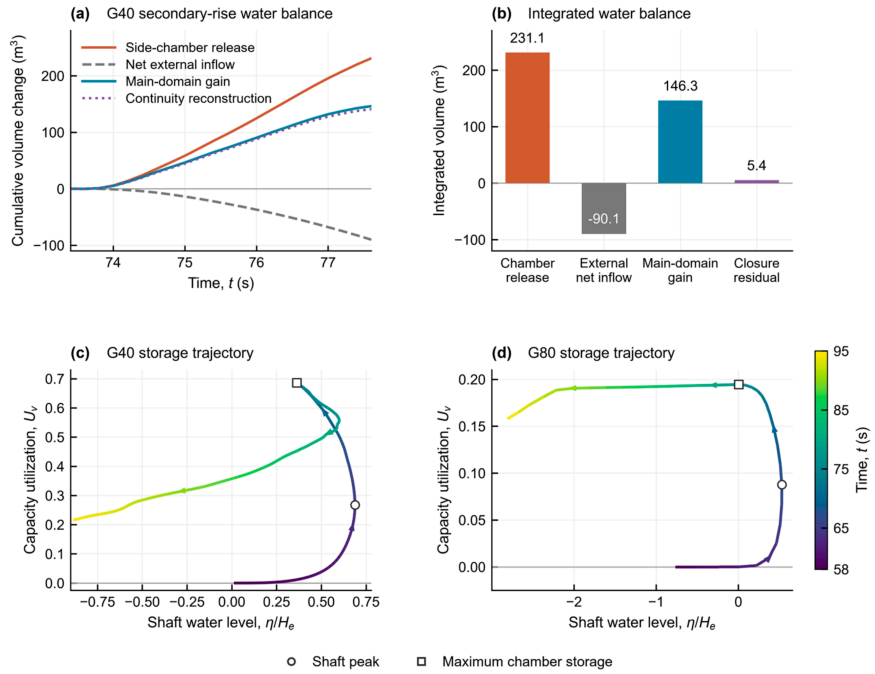

Figure 4. Water supply to the secondary rise and storage-response trajectories: (**a**) cumulative water-volume terms between the G40 intervening minimum and secondary peak; (**b**) integrated terms over the same interval; and (**c**,**d**) normalized shaft-level versus capacity-utilization trajectories for G40 and G80.

4.3. Spatiotemporal Association of Front Propagation and Return Flow

Figure 5 compares depth, longitudinal velocity, and equivalent sectional Fr using common distance and time axes and common color scales for each quantity. Dashed and dotted horizontal lines mark the shaft maximum and maximum chamber storage, respectively. The earliest sampled times at which the wetting front reaches the end region are approximately 63.61 s for G40 and 71 s for G80. End-region response therefore begins before the G40 shaft maximum. In G80, however, the front has reached only approximately 39 m at the shaft maximum of 67 s, well short of the 80 m end wall.

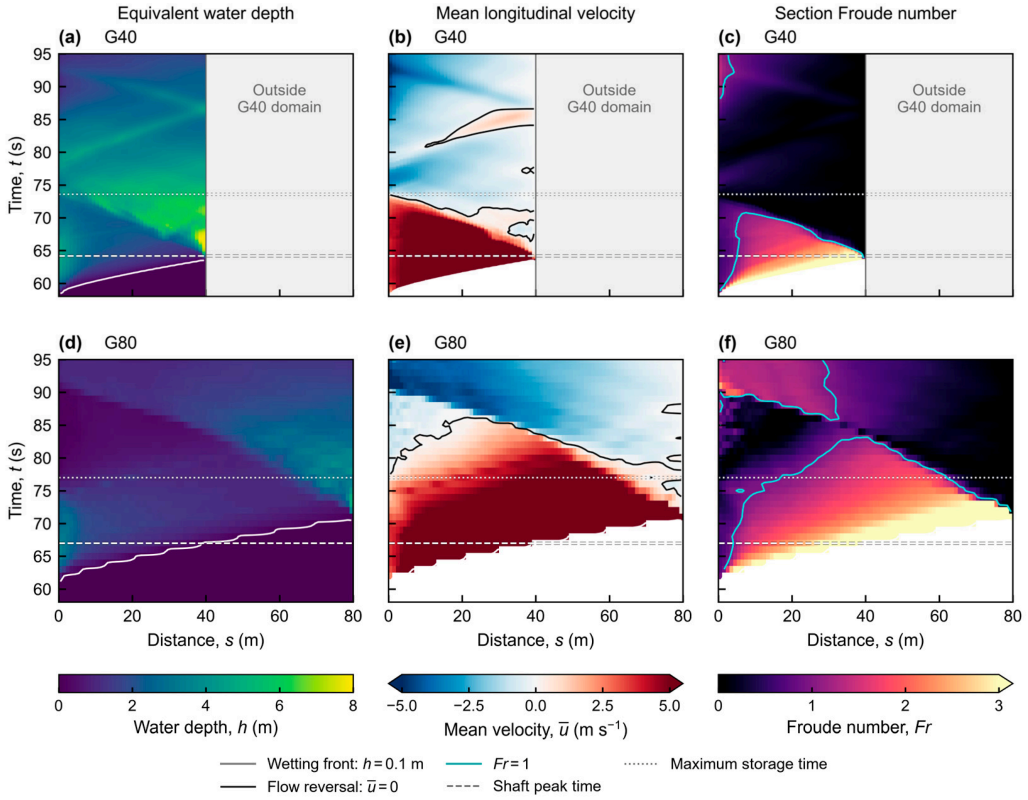

Figure 5. Spatiotemporal relationships between chamber propagation, return flow, and equivalent sectional flow state. The (**upper**) and (**lower**) rows show G40 and G80, respectively. Columns show equivalent depth, mean longitudinal velocity, and sectional Froude number. White lines denote the h = 0.1 m wetting front, black lines in the velocity maps denote ū = 0, and cyan lines denote Fr = 1.

After wetting of the G40 end region, the longitudinal depth distribution adjusts rapidly. The mean equivalent depth over the final 3 m reaches 7.61 m at approximately 67.01 s, approaching the 8 m chamber height. Subsequently, the negative-velocity region and return flow extend toward the shaft, providing spatial evidence for chamber supply during the secondary rise. End-region response is later in G80: the final-3 m mean equivalent depth reaches 3.79 m at approximately 78 s, after the shaft level has begun to recede.

The depth and velocity maps establish a continuous event sequence comprising rapid shallow-front advance, end-region rise, and subsequent reverse motion. The Fr map provides a complementary measure of the relative inertial and gravitational scales in partially filled, approximately hydrostatic segments. The Fr = 1 contour and the zero-velocity contour describe different conditions. Shallow-water critical-flow criteria are insufficient where vertical acceleration, near-full flow, or air–water mixing is pronounced; interpretation must also use the interfaces and velocity directions in Figure 6.

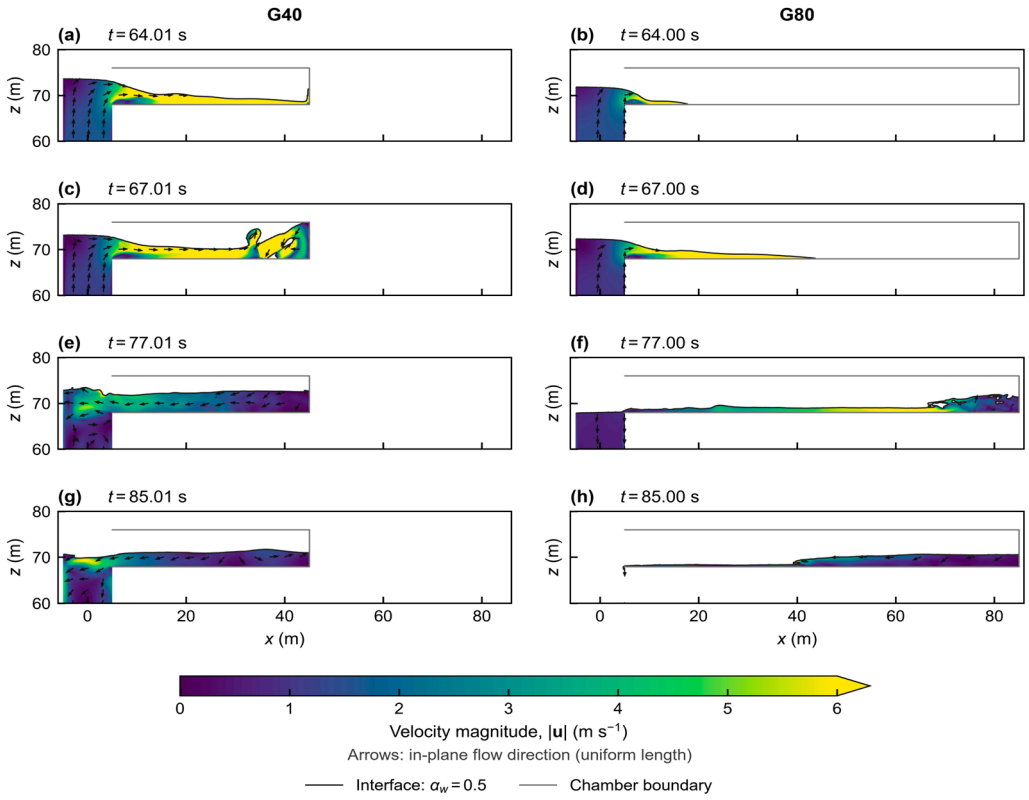

Figure 6. Centerplane free surfaces and velocity fields at corresponding physical times. The (**left**) and (**right**) columns show G40 and G80. Rows show flow-field snapshots near 64, 67, 77, and 85 s; actual times are labeled in each panel. Color represents three-dimensional velocity magnitude; black lines denote $\alpha_w = 0.5$, and equal-length arrows indicate the x–z velocity direction.

4.4. Free-Surface Shapes and Velocity-Field Evidence

Figure 6 compares both chambers at corresponding physical times and a common spatial scale. At approximately 64 s, G40 water has entered the end region, whereas G80 is dominated by a front advancing toward the end wall. At 67 s, G40 exhibits a pronounced end-region rise. Although G80 is at its shaft maximum, its wetted region has not reached the end wall. These spatial differences show why shaft maxima in different cases need not correspond to the same propagation event.

At approximately 77 s, both chamber surfaces undergo substantial adjustment, but they occupy different stages of the global response: G40 approaches its second shaft-level maximum, while G80 approaches maximum chamber storage. At 85 s, negative longitudinal motion toward the shaft and descending flow near the chamber entrance are present, and the chamber and shaft surfaces are spatially separated. These flow patterns complement the cumulative volume balance in Figure 4, showing the participation of delayed return flow in main-domain supply and the effects of end-wall reflection on local surface shape and motion.

4.5. Dominant Depth Modes and Reconstruction Error

Figure 7 summarizes the principal spatial depth structures and their coefficient evolution. The first POD mode represents 80.3% of depth-fluctuation mean-square content in G40 and 68.5% in G80. The first two modes together represent 89.7% and 86.6%, respectively. They therefore capture the dominant variations while leaving 10.3% and 13.4% of mean-square fluctuation content unresolved.

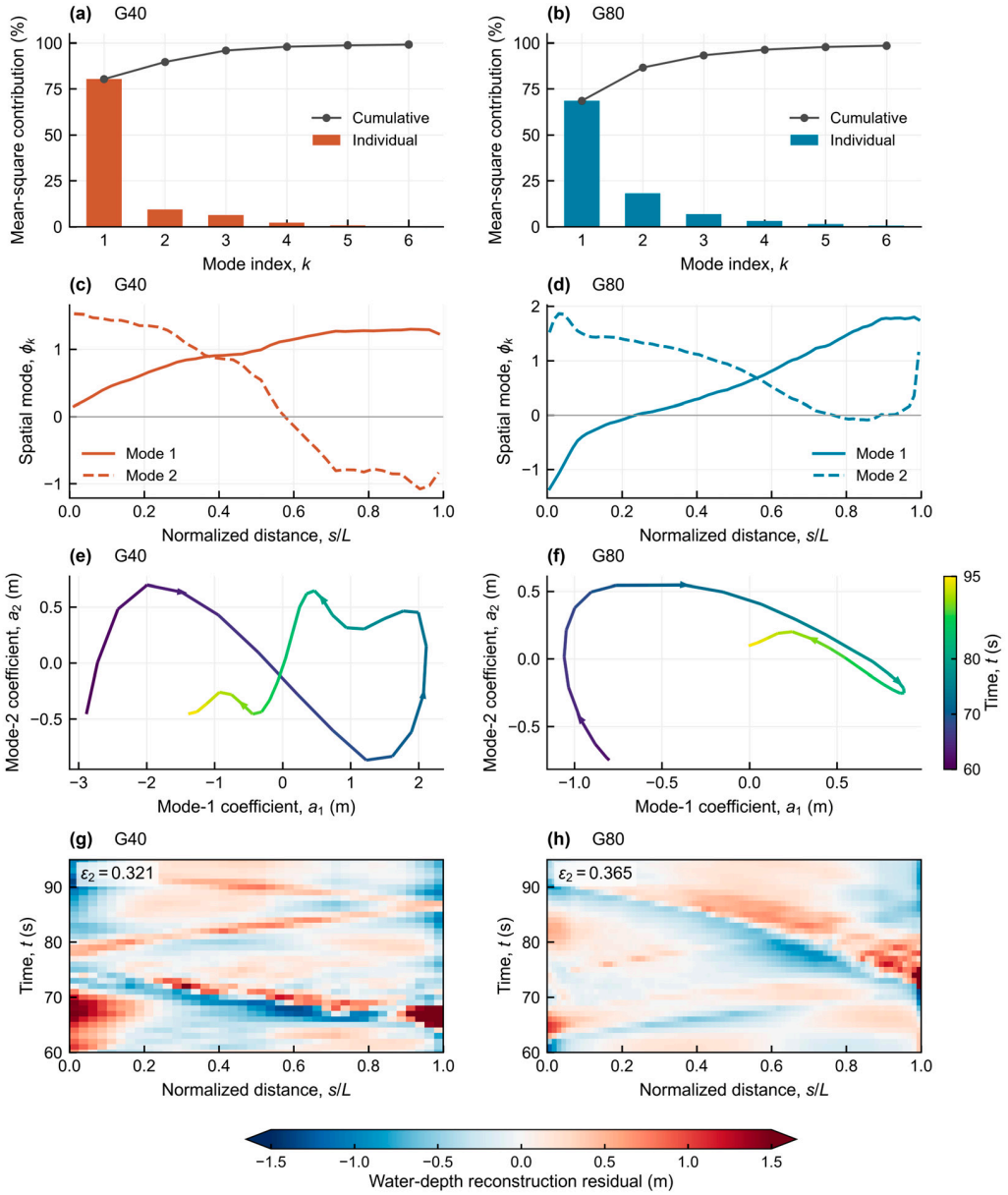

Figure 7. POD of depth fluctuations and two-mode reconstruction assessment. G40 and G80 occupy the (**left**) and (**right**) columns, respectively: (**a**,**b**) individual and cumulative fractions for the first six modes; (**c**,**d**) the first two spatial modes; (**e**,**f**) time-colored modal-coefficient trajectories; and (**g**,**h**) two-mode reconstruction residuals.

Equation (20) gives relative two-mode reconstruction errors ε_2 of 0.321 and 0.365 for G40 and G80, respectively. Figure 7g,h displays the residual distributions in space and time, explicitly identifying variations omitted from the dominant low-dimensional representation. The modal fraction and norm error are related through a square: a cumulative fraction of 89.7% does not imply a relative depth error of only 10.3%.

The G40 first mode has predominantly the same sign along the chamber and increases toward the end region, indicating broadly coherent depth adjustment with a stronger far-end response. Its second mode changes sign near s/L = 0.58, representing opposing depth variations in the near-shaft and end regions. The G80 first mode is already negative near the shaft and positive farther along the chamber, with a sign change near s/L = 0.24. This structure is consistent with asynchronous water redistribution in the longer chamber. Same-sign and opposite-sign regions characterize correlated depth changes at different

positions; coefficient trajectories describe the growth and reversal of these structures within the event. Combined with wetting-front position and flow-direction changes in Figure 5, the modes help distinguish broad filling adjustment from longitudinal depth redistribution. However, because the analysis interval contains front migration, return flow, and changes in mean storage, the POD modes cannot be identified as purely incident or reflected waves, or as natural vibration modes. Independent decompositions are compared through cumulative fractions, spatial organization, and reconstruction residuals rather than coefficient magnitude alone. Table 3 provides the corresponding metrics.

Table 3. Horizontal free-surface response and low-dimensional representation.

Metric	G40	G80
First detected front arrival at the end region (s)	63.61	71
Storage maximum lag after shaft peak (s)	9.4	10
Maximum capacity utilization (%)	68.6	19.4
Maximum final-3 m mean equivalent depth (m)	7.61	3.79
First-two-mode cumulative fraction (%)	89.7	86.6
Relative two-mode reconstruction error ε_2	0.321	0.365

Note: The wetting front is defined by h > 0.1 m. Equivalent sectional depth differs from maximum local run-up. POD errors use the same discrete space–time inner product.

5. Discussion

5.1. Different Effects of Additional Storage on Maximum and Minimum Levels

G0 and G80 exhibit different level responses under the same prescribed discharges. The 80 m chamber reduces the upward-surge maximum from 10.38 m to 4.23 m and advances its occurrence from 71 s to 67 s. However, it also lowers the downward-surge minimum from −32.74 m to −36.31 m. The respective differences, calculated before rounding, are 6.15 m and 3.56 m. Thus, the chamber reduces the upward maximum while deepening the subsequent downward excursion in this event. Maximum-level reduction does not establish simultaneous improvement of upper- and lower-level constraints, nor does it demonstrate overall attenuation of the complete surge response.

Water redistribution provides direct evidence for the upward-surge effect. At 67 s, G80 stores approximately 313.5 m^3 in the chamber. Dividing this volume by the cross-sectional area of the 10 m diameter shaft gives an equivalent water-column height of 3.99 m, close to the contemporaneous G0–G80 shaft-level difference of approximately 4.05 m. The difference between these estimates is approximately 0.06 m, indicating that the lower G80 shaft level at this time primarily corresponds to redistribution into the lateral chamber.

The G80 geometric chamber volume is 3572.9 m^3, but maximum stored water is only 694.9 m^3: 19.4% utilization, occurring 10 s after the shaft maximum. Geometric capacity is therefore not converted synchronously into actual storage during this finite-duration transient. Shaft response depends on the evolution of stored volume and its timing relative to the surge. Evaluating lateral storage requires maximum level, minimum level, and dynamic storage behavior together; the maximum level alone does not establish overall performance. This extends the distinction between geometric storage and hydraulic participation emphasized in complex surge-tank design [1,10,17].

5.2. Asynchronous Surge Response Induced by Horizontal Redistribution

The equal-volume quasi-static reference quantifies the dynamic departure associated with asynchronous chamber filling and shaft response. Over 55–100 s, G40 and G80 reach maximum positive departures of 3.12 m and 3.20 m, with $I_{d,max}$ = 0.390 and 0.400. G0 reaches only 0.14 m, with $I_{d,max}$ = 0.0176 before rounding. At the respective shaft maxima,

the departures are 2.64 m for G40 and 3.07 m for G80. Front propagation, lagged storage maxima, and these level departures provide complementary spatial and volumetric evidence: horizontal redistribution limits the instantaneous participation of lateral capacity. Shaft level and chamber storage must therefore be treated as asynchronous response quantities. This behavior is consistent with the need to account for horizontal oscillation identified by Qiu et al. [17], while the present volume-based reference quantifies the departure from instantaneous horizontal equilibration without requiring a periodic-wave assumption.

5.3. Delayed Return Flow and the Secondary Shaft-Level Rise

The G40 secondary rise has a quantitatively identified water source. The shaft reaches 5.50 m at 64.21 s, falls to 2.90 m at 73.40 s, and rises again to 4.81 m at 77.60 s, giving $K_2 = 0.734$. During the 4.20 s interval from the intervening minimum to the secondary peak, chamber release is 231.1 m^3 and net external outflow is 90.1 m^3. Their combination predicts a main-domain gain of 140.9 m^3, compared with an actual gain of 146.3 m^3. The residual is 5.4 m^3, approximately 3.7% of the actual gain. Chamber release is 2.56 times the simultaneous net external outflow and is sufficient to increase main-domain storage despite continued water removal at the external boundaries.

This continuity relation connects the secondary rise to water redistribution rather than to surface motion alone. A rising shaft level does not require renewed net external inflow: cumulative chamber return flow exceeding external outflow increases main-domain storage. Maximum G40 chamber storage occurs at 73.60 s, close to the shaft minimum between the peaks. Its subsequent decline coincides with negative longitudinal velocities and motion toward the shaft. Together, the volume balance and flow-direction evidence identify delayed chamber return flow as the direct volumetric supply for the secondary shaft-level rise. End-wall reflection can shape this redistribution, but the peak-amplitude ratio is not itself a reflection coefficient.

5.4. Physical Interpretation of Dominant Depth Structures

POD shows that a small number of correlated spatial structures dominate depth variations in both chambers, but their organization differs. The G40 first mode accounts for 80.3% of mean-square fluctuation content and has predominantly the same sign along the chamber, with stronger end-region amplitude. It represents coherent depth adjustment over much of the chamber. The second mode changes sign near $s/L = 0.58$, representing opposing changes in the near-shaft and end regions. In G80, the first mode accounts for 68.5% and changes sign near $s/L = 0.24$, indicating asynchronous near- and far-field depth adjustment. Interpreted alongside front migration and flow reversal, these structures identify broad filling adjustment and longitudinal redistribution. Their statistical interpretation follows POD applications to sloshing [18,20], while the nonperiodic filling process precludes assigning them the natural-mode identities of a stationary oscillating liquid volume.

The first two modes capture 89.7% and 86.6% of the depth-fluctuation mean-square content, with relative reconstruction errors of 0.321 and 0.365. The two-mode representation therefore retains the main correlated structures but omits localized and higher-order variations. Figure 7 locates these omissions, and the remaining 10.3% and 13.4% of mean-square content belongs to higher-order structures. Longitudinal nonuniformity I_h, POD modes and partitioned water-volume balances describe spatial dispersion, correlated organization, and actual water supply, respectively. Used together, they connect the global surge waveform with local flow evolution without interpreting statistical modal fractions as mechanical-energy fractions.

5.5. Mesh Sensitivity and Scope of Numerical Verification

A mesh-sensitivity assessment was conducted for G40 using coarse, medium, and fine meshes (Table 4). Compared with the fine mesh, the medium mesh differed by 0.07 m (1.29%) and 0.08 m (1.69%) in the primary and secondary peak levels, respectively, with corresponding peak-time differences of 0.20 s and 0.25 s. Considering these differences and the approximately twofold increase in cell count for the fine mesh, the medium mesh was adopted for G40. This assessment addresses the reported G40 surge indicators; separate mesh-refinement studies were not conducted for G0 and G80.

Table 4. Mesh-sensitivity assessment for the G40 configuration.

Mesh Level	Coarse	Medium	Fine
Number of cells ($\times 10^4$)	51.24	90.13	182.69
Primary peak level (m)	5.57	5.50	5.43
Primary peak time (s)	63.87	64.21	64.41
Secondary peak level (m)	4.86	4.81	4.73
Secondary peak time (s)	77.20	77.6	77.85

The simulations employed hexahedral meshes, the realizable k–ε model, and non-equilibrium wall functions. Dedicated y+ sensitivity tests, systematic time-step refinement, and independent experimental validation were not performed. Sampling-radius checks and the 3.7% cumulative volume-balance residual assess level-extraction sensitivity and water-volume reconstruction, respectively. These checks complement the mesh assessment but do not quantify discretization uncertainty [23]. The findings therefore provide numerical evidence for delayed storage and return flow under prescribed discharge histories, while feedback between surge-tank geometry and whole-waterway discharge remains outside the present scope [15,16].

5.6. Limitations and Future Work

Several limitations should be acknowledged. First, the present simulations employ a one-way transfer of discharge histories from the 1D hydraulic-transient model to the 3D CFD domain, without accounting for feedback between local surge responses and system-wide hydraulic transients. Second, although mesh sensitivity was assessed for G40, independent experimental validation, systematic time-step refinement, and dedicated near-wall sensitivity tests remain unavailable. Across the three configurations, the y^+ values at their respective peak-water-level instants ranged overall from 0.014 to 7.31×10^2, indicating the need for further near-wall mesh refinement and y^+ sensitivity assessment. Third, the analysis is limited to three chamber configurations under the CP4 operating scenario, restricting the general applicability of the quantitative findings. Future work will focus on developing and validating a bidirectionally coupled 1D–3D framework, allowing real-time exchange of discharge and pressure head between the two models. Additional operating conditions and experimental comparisons will be considered to improve the reliability and engineering applicability of the proposed approach.

6. Conclusions

The transient responses of throttled surge tanks without a lateral chamber and with 40 m and 80 m chambers were analyzed using VOF fields, an equal-volume quasi-static reference, partitioned water-volume balances, and POD. The following conclusions are obtained:

(1) Under identical prescribed discharges, the 80 m chamber reduces the maximum shaft level from 10.38 m to 4.23 m, a reduction of 6.15 m, and advances the peak by 4 s. It also lowers the subsequent minimum from −32.74 m to −36.31 m, a decrease of 3.56 m

calculated from unrounded values. The chamber reduces the upward-surge maximum but deepens the downward surge in this event; the maximum level alone is insufficient to evaluate its overall surge-control effect.

(2) Chamber storage lags the shaft response. G40 and G80 reach maximum storage 9.4 s and 10 s after their shaft maxima, with maximum capacity utilization of 68.6% and 19.4%. Their maximum positive dynamic level departures over 55–100 s are 3.12 m and 3.20 m, compared with 0.14 m in G0. Horizontal migration prevents instantaneous participation of lateral capacity in water redistribution, so geometric volume alone does not describe the shaft maximum.

(3) Delayed chamber return flow supplies the G40 secondary rise. Between the intervening minimum and secondary peak, chamber release is 231.1 m^3, net external outflow is 90.1 m^3, and actual main-domain gain is 146.3 m^3, with a 5.4 m^3 reconstruction residual. Return flow exceeding concurrent external outflow enables the shaft level to rise from 2.90 m to 4.81 m, giving a secondary-to-primary amplitude ratio of 0.734.

(4) End-region events and shaft maxima must be distinguished by their timing. The G80 shaft maximum occurs at 67 s, whereas the advancing wetting front reaches the end wall only at approximately 71 s. Reflection of that filling front at the end wall therefore does not generate this first shaft peak. The G40 front reaches the end region at approximately 63.61 s, before its first peak at 64.21 s; its secondary rise nevertheless has a direct volumetric source identified by the partitioned balance as chamber return flow.

(5) POD identifies different dominant depth organizations: predominantly coherent adjustment along G40 and opposing near- and far-field adjustment in G80. The first two modes represent 89.7% and 86.6% of depth-fluctuation mean-square content, with relative reconstruction errors of 0.321 and 0.365. Linking these structures to water-volume balances, front propagation, and flow reversal explains the association between global surges and local depth evolution.

(6) From an engineering perspective, lateral-chamber design should consider both maximum and minimum shaft levels rather than focusing solely on upward-surge reduction. Chamber length should also be evaluated in terms of effective storage utilization, delayed return flow, secondary surge peaks, and local water-level variations near the chamber end. In the present case, the 80 m chamber reduced the maximum shaft level by 6.15 m but lowered the subsequent minimum by 3.56 m, while utilizing only 19.4% of its geometric storage capacity. These findings suggest that increasing chamber length does not necessarily improve overall transient performance. Practical designs should therefore be assessed under representative operating conditions, with system-level hydraulic feedback considered where necessary.

Author Contributions: H.L.; methodology, H.L. and M.S.; validation, Y.L. and Z.Z.; formal analysis, R.K. and D.Y.; investigation, B.H. and J.K.; writing—original draft preparation, M.S. and Y.Y.; writing—review and editing, H.L. All authors have read and agreed to the published version of the manuscript.

Funding: This work was supported by PowerChina Northwest Engineering Corporation Limited, based on the research project "Research and Application of Key Technologies for the Engineering Characteristics of Water Conveyance and Power Generation Systems in 800 m-Class Ultra-High-Head Pumped Storage Power Stations" (Grant No. XBY-ZDKJ-2024-8).

Data Availability Statement: The numerical data generated in this study are not publicly available due to project-specific confidentiality and institutional data-sharing restrictions. Requests for access to supporting data may be directed to the corresponding author and will be considered subject to approval by the relevant institution.

Conflicts of Interest: Authors Herui Liu, Minglei Shao, Yin Liu, Ziyang Zhang, Dongshen Yang, Botao Hu, Jing Kang, and Yupeng Yan were employed by PowerChina Northwest Engineering Corporation Limited. The authors declare that this study received funding from PowerChina Northwest Engineering Corporation Limited. The funder was not involved in the study design, data collection, analysis, interpretation of data, manuscript preparation, or the decision to submit the article for publication.

Abbreviations

CFD	Computational fluid dynamics
POD	Proper orthogonal decomposition
UDF	User-defined function
VOF	Volume of fluid

References

1. Tesfay, A.H.; Lia, L.; Vereide, K. Composite surge tanks to boost hydropower flexibility. *Renew. Energy* **2025**, *251*, 123433. [CrossRef]
2. Lan, X.; Jin, J.; Xu, B.; Chen, D.; Egusquiza, M.; Kim, J.H.; Egusquiza, E.; Jafar, N.; Xu, L.; Kuang, Y. Physical model test and parametric optimization of a hydroelectric generating system with a coaxial shaft surge tank. *Renew. Energy* **2022**, *200*, 880–899. [CrossRef]
3. Kheav, K.; Duan, Y.; Egusquiza, M.; Xu, B.; Chen, D.; Egusquiza, E. Transient analysis to air chamber and orifice surge tanks in a hydroelectric generating system during the successive load rejection. *Energy Convers. Manag.* **2021**, *244*, 114449. [CrossRef]
4. Liu, Y.; Zhang, J.; Liu, Z.; Chen, L.; Yu, X. Surge wave characteristics for hydropower plant with upstream double surge tanks connected in series under small load disturbance. *Renew. Energy* **2022**, *186*, 667–676. [CrossRef]
5. Cui, Z.; Guo, W. Energy coupling and surge wave superposition of upstream series double surge tanks of pumped storage power station. *J. Energy Storage* **2024**, *101*, 113928. [CrossRef]
6. Wang, Q.; Zhang, J.; Liu, Z.; Chen, N.; Yu, X. Minimum water level in surge tank and control methodology under the combination condition of load acceptance after rejection. *Sustain. Energy Technol. Assess.* **2024**, *67*, 103846. [CrossRef]
7. Zhang, T.; Zhou, J.; Lai, X.; Huang, Y.; Li, M. Nonlinear stability and dynamic characteristics of grid-connected hydropower station with surge tank of a long lateral pipe. *Int. J. Electr. Power Energy Syst.* **2022**, *136*, 107654. [CrossRef]
8. Kim, S.; Choi, D. Dimensionless Impedance Method for General Design of Surge Tank in Simple Pipeline Systems. *Energies* **2022**, *15*, 3603. [CrossRef]
9. Kim, S. Dimensionless Pressure Response Analysis for Water Supply Pipeline Systems with or without Pumping Station. *Water* **2023**, *15*, 2934. [CrossRef]
10. Seyfeddine, M.; Vorlet, S.; Adam, N.; De Cesare, G. Holistic Design Approach of a Throttled Surge Tank: The Case of Refurbishment of Gondo High-Head Power Plant in Switzerland. *Water* **2020**, *12*, 3440. [CrossRef]
11. Zhou, J.; Palikhe, S.; Cai, F.; Liu, Y. Experimental and simulation-based investigations on throttle's head loss coefficients of a surge tank. *Energy Sci. Eng.* **2020**, *8*, 2722–2733. [CrossRef]
12. Ma, W.; Yan, W.; Yang, J.; He, X.; Yang, J.; Yang, W. Experimental and numerical investigation on head losses of a complex throttled surge tank for refined hydropower plant simulation. *Renew. Energy* **2022**, *186*, 264–279. [CrossRef]
13. Gabl, R.; Righetti, M. Design criteria for a type of asymmetric orifice in a surge tank using CFD. *Eng. Appl. Comput. Fluid Mech.* **2018**, *12*, 397–410. [CrossRef]
14. Adam, N.J.; De Cesare, G.; Schleiss, A.J. Influence of geometrical parameters of chamfered or rounded orifices on head losses. *J. Hydraul. Res.* **2019**, *57*, 263–271. [CrossRef]
15. Zhang, X.X.; Cheng, Y.G. Simulation of Hydraulic Transients in Hydropower Systems Using the 1-D-3-D Coupling Approach. *J. Hydrodyn.* **2012**, *24*, 595–604. [CrossRef]
16. Cai, F.; Cheng, Y.; Zhang, X. Approaches to guarantee accuracy of 3D CFD simulations of surge tank wave. *Eng. J. Wuhan Univ.* **2016**, *49*, 390–396. (In Chinese) [CrossRef]
17. Qiu, W.; Zhang, J.; Yu, X.; Chen, S.; Liu, Y.; Li, Y. Mathematical model and experimental validation of horizontal water level oscillations in surge tanks for hydraulic transient analysis of hydropower system. *Energy* **2025**, *329*, 136521. [CrossRef]
18. Pagliaroli, T.; Gambioli, F.; Saltari, F.; Cooper, J. Proper orthogonal decomposition, dynamic mode decomposition, wavelet and cross wavelet analysis of a sloshing flow. *J. Fluids Struct.* **2022**, *112*, 103603. [CrossRef]
19. Bardazzi, A.; Lugni, C.; Faltinsen, O.M.; Durante, D.; Colagrossi, A. Different scenarios in sloshing flows near the critical filling depth. *J. Fluid Mech.* **2024**, *984*, A73. [CrossRef]

20. Sirovich, L. Turbulence and the dynamics of coherent structures. I. Coherent structures. *Q. Appl. Math.* **1987**, *45*, 561–571. [CrossRef]
21. Hirt, C.W.; Nichols, B.D. Volume of fluid (VOF) method for the dynamics of free boundaries. *J. Comput. Phys.* **1981**, *39*, 201–225. [CrossRef]
22. Shih, T.H.; Liou, W.W.; Shabbir, A.; Yang, Z.; Zhu, J. A new k-ε eddy viscosity model for high reynolds number turbulent flows. *Comput. Fluids* **1995**, *24*, 227–238. [CrossRef]
23. Celik, I.B.; Ghia, U.; Roache, P.J.; Freitas, C.J.; Coleman, H.; Raad, P.E. Procedure for Estimation and Reporting of Uncertainty Due to Discretization in CFD Applications. *J. Fluids Eng.* **2008**, *130*, 078001. [CrossRef]

Disclaimer/Publisher's Note: The statements, opinions and data contained in all publications are solely those of the individual author(s) and contributor(s) and not of MDPI and/or the editor(s). MDPI and/or the editor(s) disclaim responsibility for any injury to people or property resulting from any ideas, methods, instructions or products referred to in the content.